Multiscale structures of Zr-based binary metallic glasses and the correlation with glass forming ability

Wu, Xuelian; Lan, Si; Wu, Zhenduo; Wei, Xiaoya; Ren, Yang; Tsang, Ho Yin; Wang, Xunli

Published in:
Progress in Natural Science: Materials International

Published: 01/08/2017

Document Version:
Final Published version, also known as Publisher's PDF, Publisher's Final version or Version of Record

Published version (DOI):
10.1016/j.pnsc.2017.08.008

Publication details:
Wu, X., Lan, S., Wu, Z., Wei, X., Ren, Y., Tsang, H. Y., & Wang, X. (2017). Multiscale structures of Zr-based binary metallic glasses and the correlation with glass forming ability. *Progress in Natural Science: Materials International*, *27*(4), 482-486. https://doi.org/10.1016/j.pnsc.2017.08.008

Progress in Natural Science: Materials International 27 (2017) 482–486

HOSTED BY

Contents lists available at ScienceDirect

Progress in Natural Science: Materials International

journal homepage: www.elsevier.com/locate/pnsmi

Original Research

Multiscale structures of Zr-based binary metallic glasses and the correlation with glass forming ability

Xuelian Wu[a], Si Lan[a,b], Zhenduo Wu[a,c], Xiaoya Wei[a,c], Yang Ren[d], Ho Yin Tsang[a], Xunli Wang[a,c,*]

[a] Department of Physics, City University of Hong Kong, 83 Tat Chee Avenue, Kowloon, Hong Kong, China
[b] Herbert Gleiter Institute of Nanoscience, School of Materials Science and Engineering, Nanjing University of Science and Technology, 200 Xiaolingwei, Xuanwu District, Nanjing, China
[c] Center of Neutron Scattering, City University of Hong Kong Shenzhen Research Institute, 8 Yuexing 1st Road, Shenzhen Hi-Tech Industrial Park, Nanshan District, Shenzhen 518057, China
[d] X-ray Science Division, Argonne National Laboratory, 9700 S. Cass Avenue, Argonne, IL 60439, USA

ARTICLE INFO

Keywords:
Metallic glasses
Glass forming ability
Densely atomic packing
Nanoscale inhomogeneity
Crystallization

ABSTRACT

Thermal behaviors and structures of three Zr-based binary glass formers, $Zr_{50}Cu_{50}$, $Zr_{64}Cu_{36}$ and $Zr_{64}Ni_{36}$, were investigated and compared using differential scanning calorimetry (DSC), transmission electron microscopy (TEM), high energy X-ray diffraction (XRD) and small angle X-ray scattering (SAXS). The high energy XRD results show that the bulk glass former $Zr_{50}Cu_{50}$ has a denser atomic packing efficiency and reduced medium-range order than those of marginal glass formers $Zr_{64}Cu_{36}$ and $Zr_{64}Ni_{36}$. Based on TEM observations for the samples after heat treatment at 10 K above their crystallization onset temperatures, the number density of crystals for $Zr_{50}Cu_{50}$ was estimated to be 10^{23}–10^{24} m^{-3}, which was four-orders higher than that in $Zr_{64}Cu_{36}$ and $Zr_{64}Ni_{36}$ metallic glasses. SAXS results indicate that $Zr_{50}Cu_{50}$ has higher degree of nanoscale inhomogeneities than those in $Zr_{64}Cu_{36}$ and $Zr_{64}Ni_{36}$ at as-cast state. The observed multiscale structures are discussed in terms of the phase stability and glass-forming ability of Zr-based binary glass formers.

1. Introduction

Metallic glasses (MGs) are formed by quenching metallic liquids to suppress crystallization [1]. It is challenging to probe the microstructure of MGs using microscopy due to artifacts induced during sample preparation [2]. Over the past decades, scattering experiments and simulations were performed to study the structure of MGs [3–7] and to provide a link between the structure and the glass formation. Short-range order (SRO) was believed to play an important role on formation of MGs upon cooling [8,9]. It was found recently that atomic re-arrangement and re-ordering at medium range scale contribute prominently to the connectivity and further densely packing for MGs [10–12].

Recently, it was proposed that MGs contain nanoscale inhomogeneous structure [13–16] beyond medium-range length scale which results in unique properties and also has a possible correlation with glass forming ability (GFA). However, the structural origin for the correlation is still unclear. Most recently, Lan et al. [17] observed a large amount of density fluctuations at nanoscale in a good ternary glass former $Zr_{46}Cu_{46}Al_8$ before crystallization using in-situ techniques. The nanoscale heterogeneous structures may link the unique crystallization behavior to the GFA in $Zr_{46}Cu_{46}Al_8$. Here, we studied atomic-to-nanoscale structures of three binary alloys, $Zr_{50}Cu_{50}$, $Zr_{64}Cu_{36}$ and $Zr_{64}Ni_{36}$, and tried to correlate the structures with GFA. These systems are chosen because of their simple chemistry and different GFAs. We observed a different crystallization behavior of a bulk binary glass former $Zr_{50}Cu_{50}$ comparing with two marginal glass formers $Zr_{64}Cu_{36}$ and $Zr_{64}Ni_{36}$. Multi-length scale characterization techniques were employed, including high energy X-ray diffraction (XRD) for atomic structure studies, e.g. atomic packing efficiency [18] and nearest neighbors using pair distribution function (PDF) analysis, small angle X-ray scattering (SAXS) for probing the density fluctuations at nanoscale.

2. Experimental methods

Glassy ribbons of $Zr_{50}Cu_{50}$, $Zr_{64}Cu_{36}$ and $Zr_{64}Ni_{36}$ (at. %) were fabricated by melt spinning with a wheel speed of ~ 30 m/s. The

Peer review under responsibility of Chinese Materials Research Society.

* Corresponding authors.
E-mail address: xlwang@cityu.edu.hk (X. Wang).

http://dx.doi.org/10.1016/j.pnsc.2017.08.008
Received 19 December 2016; Received in revised form 13 August 2017; Accepted 16 August 2017
Available online 24 August 2017

amorphous structure of as-spun samples was confirmed by wide angle X-ray scattering using a SAXSpace with Mo K_α radiation (Anton Paar, Graz, Austria), high energy XRD, and transmission electron microscope (TEM) (Phillips CM20 FEG).

The thermal stability of the amorphous as-spun ribbons was studied by a Perkin Elmer differential scanning calorimeter (DSC-7) at a constant heating rate of 10 K/min under flowing nitrogen. The glass transition temperature T_g and the crystallization temperature T_x were determined as the onsets of each event, using the two-tangents method. High energy XRD experiments were conducted at the beamline 11-ID-C, Advanced Photon Source, Argonne National Laboratory. The wavelength of the X-ray is 0.11798 Å. The diffraction spectra were acquired in transmission geometry by a 2D detector. To reduce the noise, the 2D images were azimuthally integrated. The structure factor S(Q) was obtained after the correction of detector efficiency, background scattering, polarization, absorption, and Compton scattering. The reduced pair distribution function (PDF), G(r), is obtained from the Fourier transform of S(Q): $G(r) = (2/\pi) \times \int_0^{Q_{max}} Q(S(Q)-1)\, sin(Qr)dQ$, where r is the distance in real space and $Q = 4\pi sin\theta/\lambda$. Here θ is half of the scattering angle between the incident beam and the scattered beam. λ is the X-ray wavelength.

Three MGs, were heated to the temperature ~ 10 K above T_x at a heating rate of 10 K/min in nitrogen atmosphere. They were subsequently cooled back to ambient temperature (cooling rate ~ 200 K/min). The MGs after above heat treatment in DSC were examined by TEM. The TEM foils were prepared by ion milling using a Gatan precision ion mill (PIPS) with the argon ion beam energy ~ 3 keV and the incident angle 5°. Amorphous and crystallized samples were also studied by SAXS. Thin foils with 30 μm thickness were polished for SAXS. Room temperature SAXS measurements were performed on the SAXSpace line collimation camera. The sample chamber was evacuated to vacuum during measurements to reduce the background noise. The scattering patterns were acquired in transmission geometry by a 2D detector. The 2D images were integrated azimuthally, corrected for background scattering and normalized using SAXStreat and SAXSquant software supplied by the vendor (Anton Paar). The resulting scattering intensity I(Q) was plotted as a function of the scattering vector Q.

3. Results and discussion

Fig. 1 shows the DSC traces of melt-spun Zr-Cu and Zr-Ni binary MGs conducted at a constant heating rate of 10 K/min. The glass transition and crystallization onset temperatures are marked as T_g

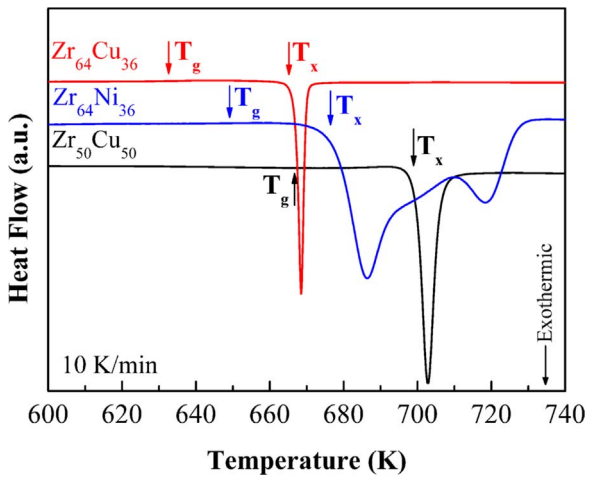

Fig. 1. DSC traces of as-spun Zr-Cu and Zr-Ni binary MGs conducted at a heating rate of 10 K/min. The glass transition temperature T_g can be referred to literatures [19,20,23] and the crystallization temperature T_x were determined as the onsets of the respective events using the two-tangents method, which are all arrowed in patterns.

Table 1
Thermophysical parameters of Zr-based binary metallic glasses.

Compositions	T_g (K)	T_x (K)	T_l (K)	T_{rg}	γ
$Zr_{50}Cu_{50}$	667	701	1226	0.544	0.370
$Zr_{64}Cu_{36}$	632	665	1284	0.492	0.347
$Zr_{64}Ni_{36}$	649	676	1283	0.506	0.350

and T_x respectively. For the Zr-Cu amorphous alloys, when the Cu content increases from 36% to 50%, T_g [19,20] increases from 632 K to 667 K. There is a similar trend for their T_x in accordance with the previous results [19,21,22]. For eutectic $Zr_{64}Ni_{36}$ alloy, T_g [23] is about 649 K. The characteristic temperatures T_g, T_x and T_l [24,25] are summarized in Table 1. From the above results, the common GFA criteria such as $\gamma = T_x / (T_g + T_l)$ [26] and $T_{rg} = T_g / T_l$ [27] parameters were evaluated. It clearly shows that the γ and T_{rg} of $Zr_{50}Cu_{50}$ are significantly higher than the corresponding values of the other two glasses, indicating a better GFA of $Zr_{50}Cu_{50}$ alloy. This is consistent with the experimental results [28–30] that $Zr_{50}Cu_{50}$ is a bulk glass former while $Zr_{64}Ni_{36}$ and $Zr_{64}Cu_{36}$ can only be made in ribbon shape. In addition, the γ and T_{rg} of $Zr_{64}Ni_{36}$ are slightly higher than that of $Zr_{64}Cu_{36}$, implying a better GFA of $Zr_{64}Ni_{36}$ than $Zr_{64}Cu_{34}$.

The crystallized samples were prepared by the heat treatment as described in the experimental part. Their microstructures were studied by TEM. Fig. 2(a)-(c) shows the TEM bright filed (BF) images of the crystallized $Zr_{50}Cu_{50}$, $Zr_{64}Cu_{36}$, and $Zr_{64}Ni_{36}$. The insets of Fig. 2(a)-(c) are the corresponding selected area electron diffraction (SAED) patterns. For $Zr_{50}Cu_{50}$, the SAED has only several sharp rings. No obvious diffraction spots are found, indicating the existence of a finely dispersed nanocrystals with random orientations. The BF image further confirms that there are a lot of black and grey crystalline spherical particles embedded in the amorphous matrix. In addition, the size distribution of the nanoscale crystalline particles determined from the BF image is shown in Fig. 2(d). From Fig. 2(d), the mean crystalline particle size is found to be about 16.0 nm. In $Zr_{64}Ni_{36}$, however, several bright diffraction spots are found in SAED, indicating there exist a small amount of crystals with large size. The corresponding BF image also confirms that the crystal size is large (~ 200 nm) and the amount is small. In $Zr_{64}Cu_{36}$, the diffraction spots are even sharper than those of the $Zr_{64}Ni_{36}$. Interestingly, large black areas ~ 100 nm (as indicated by the red dashed lines in Fig. 2(b) in the crystalline precipitates) can be observed, which is consistent with the clear diffraction spots in the SAED. The BF image and SAED of crystalline $Zr_{64}Cu_{36}$ alloy illustrated that the crystals can grow very large and can maintain the same crystal orientation.

The crystallized $Zr_{50}Cu_{50}$ was then studied by SAXS and the resulting I(Q) is shown in Fig. 3(a). From TEM observation, the crystalline particles are roughly in a spherical shape. The real space pair distance distribution function p(r) or PDDF can be obtained by the equation $p(r) = (1/2\pi^2) \times \int_0^\infty I(Q)Qrsin(Qr)dQ$ [31]. Fig. 3(b) shows the p(r) of crystalline particles obtained by the indirect Fourier transformation of I(Q) using GIFT (Anton Paar). The average diameter of nanocrystals in $Zr_{50}Cu_{50}$ is found to be ~ 18 nm, which agrees well with the size determined by TEM.

According to the TEM and SAXS results, the estimated diameter of a crystal in $Zr_{50}Cu_{50}$ is about 16–18 nm. By calculation, the crystal's volume $V_{crystal}$ is about 2×10^3 nm^3. Thus, for a fully crystallized $Zr_{50}Cu_{50}$, the number density of crystals can be estimated by $1/V_{crystal}$, which is about 10^{23}–10^{24} m^{-3}. This is 4 orders higher than the estimated crystal number density in the crystallized $Zr_{64}Cu_{36}$ and $Zr_{64}Ni_{36}$. Since all three MGs were prepared by similar methods, the significant increase of crystal density should not come from the quenched-in impurities. What's

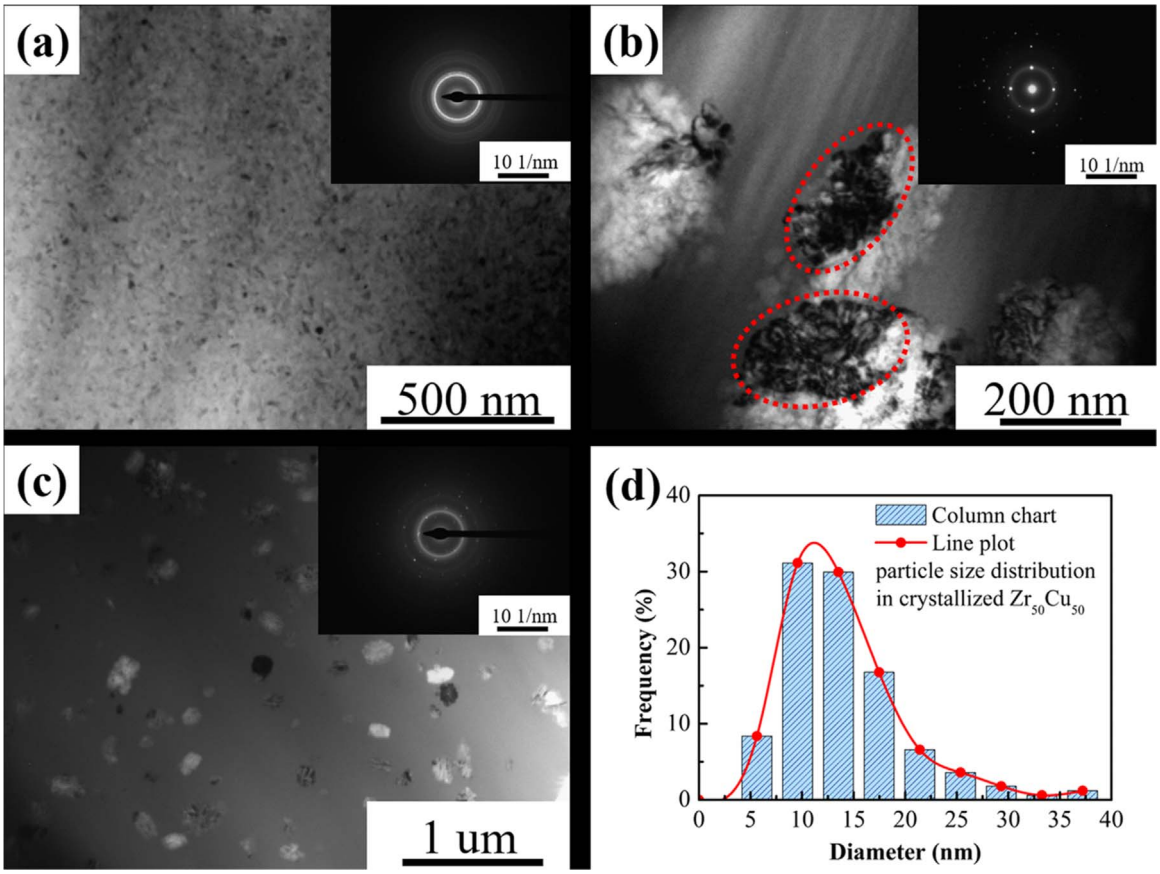

Fig. 2. TEM bright filed images of the heat treated (a) $Zr_{50}Cu_{50}$, (b) $Zr_{64}Cu_{36}$, and (c) $Zr_{64}Ni_{36}$, together with corresponding selected area electron diffraction patterns. (d) Particle size distribution for $Zr_{50}Cu_{50}$. The black regions inside the red line in (c) indicate several grains with the same orientation.

more, it is unlikely to have so many impurities in the alloys. Another explanation is that phase separation occurs before crystallization [32,33]. However, no sign of phase separation prior crystallization was observed in $Zr_{50}Cu_{50}$ alloy system.

To understand the good GFA and different crystallization process of $Zr_{50}Cu_{50}$, we performed high energy XRD and SAXS to study the atomic and nanoscale structures of their amorphous state. Fig. 4(a) shows the structure factors S(Q) obtained by high energy XRD of all three MGs. All of them exhibit a strong first peak accompanied by dramatically declined oscillations at the high Q side, a typical character of an amorphous state. The peak position Q_1 [34] of the first sharp diffraction peak of S(Q) was determined, and the results are presented in Table 2. Based on the Q_1 values, the atomic volume (V_a) was calculated by the formula $Q_1 \times V_a^{0.433} = 9.3$, appended in Table 2 [10]. These values nearly equal to those obtained from the mass density ρ_m [10,19] (shown in the bracket as a reference). The packing fraction (φ) was calculated by the relationship of $\varphi = \sum_i \frac{4}{3} c_i \pi R_i^3 / V_a$, as described in Ref. [18], where R_i is the atomic radius of the i^{th} element [35], c_i is the atomic fraction. It is also summarized in Table 2. From the high energy XRD data, the $Zr_{50}Cu_{50}$ metallic glass has the highest packing fraction among all. The trend of packing fraction of the three glasses roughly follows the trend of GFA ($Zr_{50}Cu_{50}$ > $Zr_{64}Ni_{36}$ > $Zr_{64}Cu_{36}$). Because of the highest packing fraction, the atomic diffusivity in $Zr_{50}Cu_{50}$ is believed to be slow.

The full width at half maximum (FWHM) of the first peak in S(Q) is also shown in Table 2. The first peak of $Zr_{50}Cu_{50}$ is found to be broader than the others. The broader peak indicates a reduced medium range order (MRO) in real space [10]. Combined the FWHM results, the good GFA of $Zr_{50}Cu_{50}$ is found to correlate well with the reduced MRO. To obtain a better understanding of the atomic structures of the three glasses, the corresponding PDFs were obtained, as shown in Fig. 4(b). The PDFs reveal SRO and MRO up to 20 Å. The main features of the second and higher PDF peaks of $Zr_{64}Cu_{36}$ and $Zr_{64}Ni_{36}$ are similar, revealing the similar MRO of the two glasses. However, there is a significant difference in the PDF of $Zr_{50}Cu_{50}$ up to 20 Å [36]. The peak positions of the PDF of $Zr_{50}Cu_{50}$ deviate from the other two glasses as the r increases, indicating a different MRO in the $Zr_{50}Cu_{50}$. PDF results also show the peaks damp faster in $Zr_{50}Cu_{50}$, showing that the $Zr_{50}Cu_{50}$ metallic glass has the most reduced MRO. The inset of Fig. 4(b) shows an enlarged profile of the first PDF peak, which contains the structure information of the nearest neighbors, with different interatomic distances inside. The first peak splits into two maxima. It reveals a similar short range atomic environment of $Zr_{64}Cu_{36}$ and $Zr_{64}Ni_{36}$, but a different local environment in $Zr_{50}Cu_{50}$.

SAXS was used to study nanoscale structures of the three MGs. Fig. 4(c) illustrates SAXS profiles of as-spun $Zr_{50}Cu_{50}$, $Zr_{64}Cu_{36}$, and $Zr_{64}Ni_{36}$ glasses. All three curves show a significant increase of intensity at low Q, which is attributed to the scattering from the sample imperfections. Interestingly, $Zr_{50}Cu_{50}$ shows a noticeable higher intensity in a broad Q range (from 0.1 nm^{-1} to 1 nm^{-1}) in comparison with $Zr_{64}Cu_{36}$ and $Zr_{64}Ni_{36}$ MGs. The enhanced scattering in this Q range comes from a larger electron density difference in the range from several nanometers to tens of nanometers in real space. In other words, the SAXS results indicate $Zr_{50}Cu_{50}$ has a highest degree of nanoscale heterogeneities among the three MGs.

The above experimental results show that $Zr_{50}Cu_{50}$ has a higher atomic packing fraction, a damped MRO, and a higher degree of nanoscale heterogeneities. In earlier studies, Lan, et al. [37,38] proposed that local ordering (short-to-medium range ordering) in

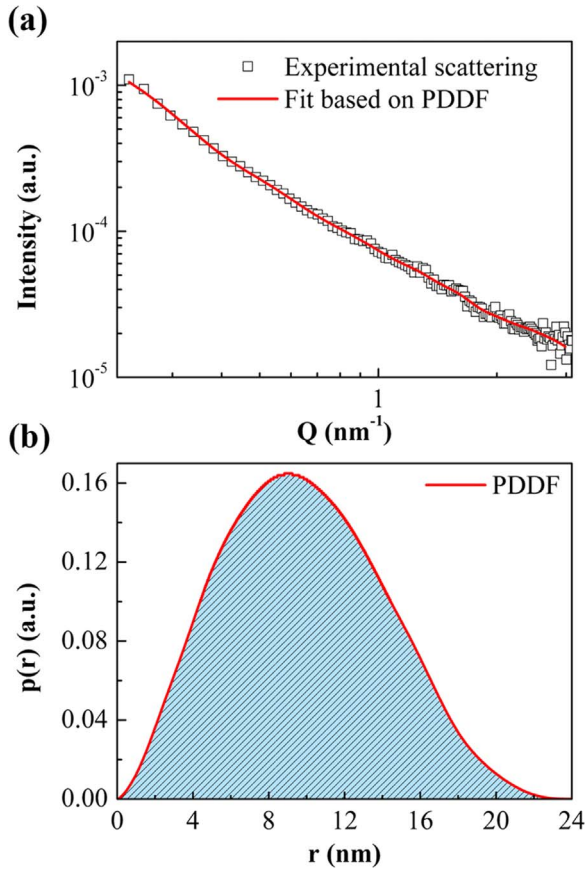

Fig. 3. (a) SAXS profiles and fitting results of the crystallized $Zr_{50}Cu_{50}$ metallic glass; (b) PDDF of the crystallized $Zr_{50}Cu_{50}$ metallic glass obtained from the SAXS result in (a) by indirect Fourier transformation.

amorphous Pd-Ni-P alloys may correspond to the nanoscale amorphous phase separation, in which the metallic glass alloy separate into two or more amorphous regions in nanometer scale. The scenario of phase separation has also been proposed in the good glass former $Zr_{50}Cu_{50}$ [39]. According to the two-order parameter model [40], the competition between the collective arrangement of MRO and the density would be responsible for the tendency of amorphous phase separation or poly-amorphous phase transition [41,42], which results in higher degree of heterogeneities in $Zr_{50}Cu_{50}$. The enhanced spatial heterogeneity is a possible reason for the large number density of small nanocrystals in $Zr_{50}Cu_{50}$. In addition, high energy XRD shows the $Zr_{50}Cu_{50}$ has a large atomic packing fraction. The densely packed structure may cause a lower diffusion rate in the $Zr_{50}Cu_{50}$ glass. The lower diffusion rate can result in a lower growth rate of the nanocrystals. This is in consistent with the TEM observation that the crystal growth rate in $Zr_{50}Cu_{50}$ is the lowest among all. The combination of a high degree of structural heterogeneities and a low crystal growth rate is the possible reason of the high density of nanocrystals in $Zr_{50}Cu_{50}$. Recently, Lan et al. [17] showed that the crystallization behavior of a good glass former $Zr_{46}Cu_{46}Al_8$ was characterized by site-saturated nucleation followed by slow growth. The high density of nucleation sites also points to a high degree of structural fluctuation in the glassy state in the $Zr_{46}Cu_{46}Al_8$ alloy.

4. Conclusions

The GFA of bulk binary glass former $Zr_{50}Cu_{50}$ has been found to correlate well with the densely atomic packing and the reduced MRO as well as nanoscale inhomogeneity. Upon heating, the $Zr_{50}Cu_{50}$ MG

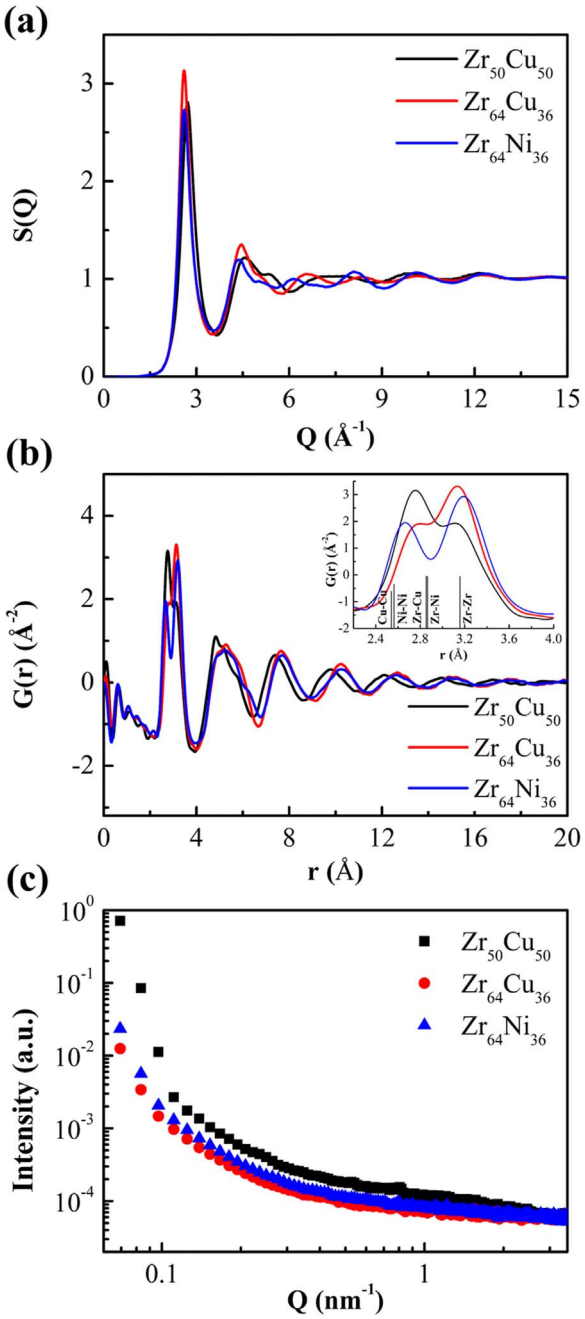

Fig. 4. (a) S(Q) of amorphous Zr-Cu and Zr-Ni MGs obtained from synchrotron X-ray diffraction; (b) Their corresponding pair distribution function G(r), (Inset: close-up of the first peak); (c) The SAXS results of as-spun MGs.

Table 2
Structural parameters of amorphous Zr-based binary metallic glasses. Atomic volume V_a was obtained from the relationship [10]. Q_1 represents the peak position of the first sharp diffraction peak of structure factor S(Q). Atomic volume V_a was also calculated from mass density ρ_m [10,19] shown in brackets. The packing fraction φ was calculated using atomic volume divided by the total volume [18]. The full width at half maximum (FWHM) was calculated from the first peak of S(Q).

Compositions	Q_1 (Å^{-1})	ρ_m (g/cm^3)	V_a (Å^3)	φ	FWHM (Å^{-1})
$Zr_{50}Cu_{50}$	2.720	7.408	17.10 (17.35)	0.734 (0.723)	0.526
$Zr_{64}Cu_{36}$	2.593	7.01	19.10 (19.25)	0.715 (0.710)	0.442
$Zr_{64}Ni_{36}$	2.611	6.98	18.80 (18.92)	0.731 (0.726)	0.484

exhibits a rather different crystallization process, where the number density of crystals generated is estimated to be 10^{23}–10^{24} m^{-3}, which is 4 orders of magnitudes higher than that in $Zr_{64}Cu_{36}$ and $Zr_{64}Ni_{36}$ MGs.

Acknowledgements

This work was supported by Shenzhen Science and Technology Innovation Commission (Grant No. R-IND8701) and by a grant from the Croucher Foundation (CityU Project No. 9500020). XLW and SL acknowledge partial support by the National Natural Science Foundation of China, No. 51501090 and No. 51571170 and "The Fundamental Research Funds for the Central Universities," No. 30915015103. The authors acknowledge the use of Advanced Photon Source, a U.S. Department of Energy (DOE) Office of Science User Facility operated for the DOE Office of Science by Argonne National Laboratory under Contract No. DE-AC02-06CH11357.

References

[1] H. Jones, C. Suryanarayana, J. Mater. Sci. 8 (1973) 705–753.
[2] D. Nagahama, T. Ohkubo, K. Hono, Scr. Mater. 49 (2003) 729–734.
[3] X.L. Wang, J. Almer, C.T. Liu, Y.D. Wang, J.K. Zhao, A.D. Stoica, D.R. Haeffner, W.H. Wang, Phys. Rev. Lett. 91 (2003) 265501.
[4] L. Yang, M.K. Miller, X.L. Wang, C.T. Liu, A.D. Stoica, D. Ma, J. Almer, D. Shi, Adv. Mater. 21 (2009) 305–308.
[5] H.W. Sheng, W.K. Luo, F.M. Alamgir, J.M. Bai, E. Ma, Nature 439 (2006) 419–425.
[6] Y.Q. Cheng, E. Ma, H.W. Sheng, Phys. Rev. Lett. 102 (2009) 245501.
[7] A. Hirata, P.F. Guan, T. Fujita, Y. Hirotsu, A. Inoue, A.R. Yavari, T. Sakurai, M.W. Chen, Nat. Mater. 10 (2011) 28–33.
[8] K.F. Kelton, G.W. Lee, A.K. Gangopadhyay, R.W. Hyers, T.J. Rathz, J.R. Rogers, M.B. Robinson, D.S. Robinson, Phys. Rev. Lett. 90 (2003) 195504.
[9] D.B. Miracle, Nat. Mater. 3 (2004) 697–702.
[10] D. Ma, A.D. Stoica, X.L. Wang, Nat. Mater. 8 (2009) 30–34.
[11] S. Lan, M. Blodgett, K.F. Kelton, J.L. Ma, J. Fan, X.L. Wang, Appl. Phys. Lett. 108 (2016) 211907.
[12] J. Ding, E. Ma, M. Asta, R.O. Ritchie, Sci. Rep. 5 (2015) 17429.
[13] J.C. Ye, J. Lu, C.T. Liu, Q. Wang, Y. Yang, Nat. Mater. 9 (2010) 619–623.
[14] T. Ichitsubo, E. Matsubara, T. Yamamoto, H.S. Chen, N. Nishiyama, J. Saida, K. Anazawa, Phys. Rev. Lett. 95 (2005) 245501.
[15] Z. Wang, B.A. Sun, H.Y. Bai, W.H. Wang, Nat. Commun. 5 (2014) 5823.
[16] H. Wagner, D. Bedorf, S. Kuchemann, M. Schwabe, B. Zhang, W. Arnold, K. Samwer, Nat. Mater. 10 (2011) 439–442.
[17] S. Lan, X.Y. Wei, J. Zhou, Z.P. Lu, X.L. Wu, M. Feygenson, J. Neuefeind, X.L. Wang, Appl. Phys. Lett. 105 (2014) 201906.
[18] D. Ma, A.D. Stoica, X.L. Wang, Appl. Phys. Lett. 91 (2007) 021905.
[19] N. Mattern, A. Schops, U. Kuhn, J. Acker, O. Khvostikova, J. Eckert, J. Non-Cryst. Solids 354 (2008) 1054–1060.
[20] I. Kalay, M.J. Kramer, R.E. Napolitano, Metall. Mater. Trans. A 42 (2011) 1144–1153.
[21] Z. Altounian, G.H. Tu, J.O. Stromolsen, J. Appl. Phys. 53 (1982) 4755–4760.
[22] K. Georgarakis, A.R. Yavari, D.V. Louzguine-Luzgin, J. Antonowicz, M. Stoica, Y. Li, M. Satta, A. LeMoulec, G. Vaughan, A. Inoue, Appl. Phys. Lett. 94 (2009) 191912.
[23] K. Georgarakis, A.R. Yavari, M. Aljerf, D.V. Louzguine-Luzgin, M. Stoica, G. Vaughan, A. Inoue, J. Appl. Phys. 108 (2010) 023514.
[24] H. Okamoto, J. Phase Equilib. Diffus. 28 (2007) 409.
[25] H. Okamoto, J. Phase Equilib. Diffus. 33 (2012) 417–418.
[26] Z.P. Lu, C.T. Liu, Acta Mater. 50 (2002) 3501–3512.
[27] Z.P. Lu, Y. Li, S.C. Ng, J. Non-Cryst. Solids 270 (2000) 103–114.
[28] D.H. Xu, B. Lohwongwatana, G. Duan, W.L. Johnson, C. Garland, Acta Mater. 52 (2004) 2621–2624.
[29] Y. Li, Q. Guo, J.A. Kalb, C.V. Thompson, Science 322 (2008) 1816–1819.
[30] G. Duan, D.H. Xu, Q. Zhang, G.Y. Zhang, T. Cagin, W.L. Johnson, W.A. Goddard, Phys. Rev. B 71 (2005) 224208.
[31] A. Guinier, G. Fournet, John Wiley, New York, 1955.
[32] A.K. Gangopadhyay, T.K. Croat, K.F. Kelton, Acta Mater. 48 (2000) 4035–4043.
[33] B. Lohwongwatana, J. Schroers, W.L. Johnson, Phys. Rev. Lett. 96 (2006) 075503.
[34] W. Jiao, X.L. Wang, S. Lan, S.P. Pan, Z.P. Lu, Appl. Phys. Lett. 106 (2015) 061910.
[35] T. Egami, Y. Waseda, J. Non-Cryst. Solids 64 (1984) 113–134.
[36] A.R. Yavari, Nature 439 (2006) 405–406.
[37] S. Lan, Y.L. Yip, M.T. Lau, H.W. Kui, J. Non-Cryst. Solids 358 (2012) 1298–1302.
[38] Z.D. Wu, X.H. Lua, Z.H. Wu, H.W. Kui, J. Non-Cryst. Solids 385 (2014) 40–46.
[39] R. Schulz, K. Samwer, W.L. Johnson, J. Non-Cryst. Solids 61–62 (1984) 997–1002.
[40] H. Tanaka, J. Phys. Condens. Matter 10 (1998) 207–214.
[41] S. Lan, M. Blodgett, K.F. Kelton, J.L. Ma, J. Fan, X.L. Wang, Appl. Phys. Lett. 108 (2016) 211907.
[42] S. Lan, Y. Ren, X.Y. Wei, B. Wang, E.P. Gilbert, T. Shibayama, S. Watanabe, M. Ohnuma, X.L. Wang, Nat. Commun. 8 (2017) 14679. http://dx.doi.org/10.1038/ncomms14679.